

requires detailed validation, for example it may be compromised by metal fulvic complexes adsorbing directly to the resin, it is clear that this new speciation measurement is not dependent on the nature of the resin providing the reaction between free metal and resin is fast. Other sorbent or immobilized ligands, which could compete effectively with the solution ligands and would not adsorb metal complexes, could be used and the same species would be measured.

To test these principles, gel assemblies were constructed using a 10.5 cm diameter, 1.3 cm total thickness perspex disc containing layers of gel and resin (Fig. 1). The gel was exposed through a 5.0 cm diameter window; a set of screws and an 'o'-ring prevented ingress of water to the side or back of the gel while holding the layers of gel firmly onto the perspex backing. After casting, polyacrylamide gel was hydrated in water for at least 24 h to ensure dimensional stability before use. The resin was embedded in a separate $\sim 150\text{ }\mu\text{m}$ -thick gel as a single plane of approximately close-packed beads. After immersion, the gel layer was peeled off, metal extracted from the resin layer with 1 ml of 2 M HNO_3 and measured using atomic absorption spectroscopy. Self-diffusion coefficients for Zn for the appropriate temperatures⁹ were used. Gel thicknesses should be entirely reproducible as they are determined by casting. The thickness of the hydrated gel was measured by a travelling microscope and was accurate to better than 4%.

Laboratory exposures of gel assemblies to stirred solutions of $\sim 10^{-7}\text{ M Zn(NO}_3)_2$, with and without added NaCl (0.5 M), showed that the concentration of metal measured in the resin layer could be predicted quantitatively (97–100%) by equation (4). Measurements of Zn in pH-adjusted sea-water, covering the pH range 4.8–7.8, by direct anodic stripping voltammetry without sample pretreatment and by gels exposed to stirred solutions were in good agreement (Fig. 2a). In an unstirred solution recovery was only 60%, indicating that mass transport was partly limited by the DBL in solution. On lowering the pH to 2.5, recovery was greatly reduced, consistent with the properties of Chexel 100.

In natural sea water, particles adhere to the gel surface and so may affect the inward diffusion of metal ions. Covering the gel with a 100 μm -thick, 0.45- μm pore size cellulose nitrate membrane prevented the particles sticking. Diffusion through the filter was indistinguishable from that through a similar thickness gel. Varying the time of *in situ* immersion in sea water (Fig. 2b) resulted in mass increasing linearly with time. As the tidal current varied from 0 to ~ 4 knots during this time, the thickness of the DBL will also vary. Consequently the linear response indicates that the gel thickness is dominating the control of mass transport confirming the assumption that the DBL is negligible. The mean concentration from these measurements was very reproducible at $11.9 \pm 0.4\text{ nM}$ as compared to $26.5 \pm 2.8\text{ nM}$ from seven samples taken at hourly intervals and measured by anodic stripping voltammetry after acidification to pH 2 and exposure to ultraviolet irradiation. A difference is to be expected if it is considered that DGT only measures labile species and therefore will exclude kinetically inert organic species and large colloids.

To investigate further the effect of the gel layer, assemblies of different gel thicknesses, covered by 100 μm -thick filters, were exposed to sea water for 320 min. Consistent with equation (2), the mass measured in the resin was inversely proportional to the total thickness of the filter and gel layer (Fig. 2c), except for when there was no gel layer and only a 100- μm filter was used. The reduced recovery for the 100- μm case can be used to provide an estimate of the mean effective thickness of the DBL of 30 μm .

These measurements demonstrate that the theoretical principles of the DGT technique hold for practical *in situ* use. By using a gel to define the diffusion layer thickness, the mass transport of the system and the criteria for defining the measured species are effectively defined. Using a 0.5-mm diffusion layer, as in these experiments, a concentration factor of 72 is obtained by a 1 h immersion. Such a procedure using simple equipment

immediately overcomes most contamination problems that beset trace metal measurements. The technique is suitable for deployment from aboard ship and a time of 1 h is appropriate for sensing temporal changes in trace metal concentrations in sea water. Changes during tidal cycles could potentially be measured, especially as the technique is independent of ionic strength and pH. Moreover, as the capacity of the resin should allow 3 months immersion in relatively contaminated coastal waters before saturation is reached, the device can readily be used to provide a long-term (weeks, months) integrated record of trace metal concentrations. The limiting factor will most likely be the effects of biofouling, but there is certainly potential for the use of DGT as a chemical alternative to shellfish for providing integrated records of trace metal pollution¹². DGT is in principle applicable to most trace metals in any non-acid aqueous medium, although the detailed use in complicated solutions like fresh waters, where colloidal material is very important, requires further testing. This new measurement principle can theoretically be applied to any component, including organics, that can readily diffuse through a gel layer and be consumed by an active component in a backing layer. □

Received 19 July; accepted 22 December 1993.

1. Tercier, M. L., Buffle, J., Zirino, A. & De Vitre, R. R. *Analytica chim. Acta* **237**, 429–437 (1990).
2. Davey, E. W. & Soper, A. E. *Limnol. Oceanogr.* **20**, 1019–1023 (1975).
3. Buffle, J. *Complexation Reactions in Aquatic Systems* (Ellis-Horwood, Chichester, 1988).
4. Morrison, G. M. P. *Envir. Technol. Lett.* **8**, 393–402 (1987).
5. Davison, W., Grime, G. W., Morgan, J. A. W. & Clarke, K. *Nature* **352**, 323–325 (1991).
6. W. E. Reinlove. *J. phys. Chem.* **96**, 10–19 (1993).
7. Santschi, P., Hohener, P., Benoit, G. & Buchholtz-ten Brink, M. *Mar. Chem.* **30**, 269–315 (1990).
8. Chrambach, A. *The Practice of Quantitative Gel Electrophoresis* (VCH, Weinheim, 1985).
9. Li, Y. & Gregory, S. *Geochim. cosmochim. Acta* **38**, 703–714 (1974).
10. Snodgrass, W. J. in *Sediments and Water Interactions* (ed. Sly, P. G.) (Springer, New York, 1986).
11. Davison, W. *J. Electroanal. Chem.* **87**, 395–404 (1978).
12. Lopez, P. B., Bajdik, C. D., Belkhole, S. P., Jackson, S. E. & Longerich, H. P. *Arch. Envir. Contam. Tox.* **21**, 409–420 (1991).

ACKNOWLEDGEMENTS. We thank K. Reid, G. Johnson and G. Jones for help with sampling, and the UK Natural Environment Research Council for financial support.

Western boundary currents in the atmosphere of Mars

M. M. Joshi, S. R. Lewis, P. L. Read & D. C. Catling

Atmospheric, Oceanic and Planetary Physics, Clarendon Laboratory, Parks Road, Oxford OX1 3PU, UK

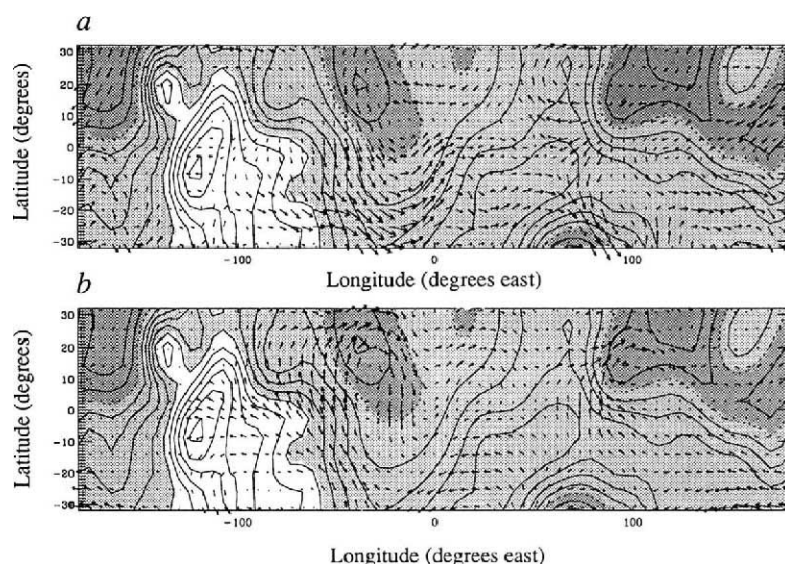
WESTERN boundary currents (WBCs) are an intensification of north–south flow adjacent to an eastward-facing meridional boundary. Although most familiar in the oceans (where the Gulf Stream is the best known example), WBCs also occur in the Earth's troposphere, the main example being the East African Jet¹, which is thought to play an important role in the Asiatic monsoon. Here we identify boundary currents in a different geophysical context: a numerical simulation of the atmosphere of Mars. In our simulation, WBCs exist in association with significant cross-equatorial flow and the presence of equatorial martian topography, which has vertical scale far exceeding terrestrial relief². The intensity and width of these currents depend on model parameters, notably the surface drag. From a comparison of our results with other martian models we suggest that WBCs have already been simulated, although they were not previously identified as such³. The available observational evidence appears to be consistent with the presence of martian WBCs, which may be important in the generation of global and great dust storms.

FIG. 1 *a, b*, Two longitude–latitude plots for Mars, showing 15 sol time-mean wind vectors (arrows) in the lowest model level superimposed on topography contours. The contours are at 1 km intervals, with the zero contour dotted. Regions below this are shaded dark grey, regions in the interval 0–5 km are shaded light grey and regions above 5 km elevation are unshaded. In both cases the longest arrow represents a velocity of 30 m s^{-1} . *a*, Results from a run simulating northern winter solstice, and *b*, results simulating southern winter solstice, both runs having been carried out with $\tau = 10$ sol and T21 resolution which signifies model fields being truncated in spectral space so that the maximum retained total (longitudinal + latitudinal) wavenumber or spherical harmonic is 21. In both cases the larger of the two WBCs is at longitude 50° W on the eastern flank of the Tharsis plateau, which stretches from 50° W to 120° W . Another smaller WBC is present on the eastern side of Syrtis Major, at 80° E , this current being more intense in southern winter (*b*). A return flow is shown in the region 0° – 20° W . The major topographic features are Tharsis (130° – 70° W , 20° S – 10° N), Chryse Planitia (centred at 40° W , 25° N), Noachis (centred at 10° E , 25° S), Hellas (80° E , 30° S) and Syrtis Major (centred at 70° E , 10° N).

The simplest theoretical context in which WBCs occur is represented by the linear frictionless shallow-water equations⁴ in the presence of a meridional boundary, and in which the magnitude of the Coriolis parameter f varies with latitude y as $f = f_0 + \beta y$, f_0 and β being constants. On starting from rest and integrating forward in time, a steady state is reached everywhere except at the western boundary, where the width of the WBC produced will decay until infinitesimally small. In reality, of course, one of two things will happen to make the width of the jet tend to a non-zero limiting value: either friction dominates and the width of the jet tends approximately to $O(1/\tau\beta)$, where O means “of order” and τ is the characteristic timescale over which the friction acts; or non-linear inertial effects dominate and the width of the jet tends to $O((U/\beta)^{1/2})$ where U is a typical r.m.s. wind strength. Although such a model is much simpler than a real system, it can be helpful in determining whether a more realistic WBC is controlled by frictional or inertial forces. In the case of the equatorial region of Mars, where $\beta \approx 4 \times 10^{-11} \text{ m}^{-1} \text{ s}^{-1}$ and 1° of longitude $\approx 60 \text{ km}$, it would be expected that a frictional WBC would have width $O(5/\tau)^\circ$ of longitude, where τ is measured in sols (1 sol is a martian day $\approx 24.66 \text{ h}$) and an inertial WBC would have width $O(3\sqrt{U})^\circ$ of longitude.

The numerical model used for this investigation is a simple general circulation model (SGCM) originally developed by Hoskins and Simmons⁵, which solves the hydrostatic primitive equations of dynamical meteorology on a sphere. In the vertical, the model uses the σ -coordinate system (σ is pressure divided by surface pressure) in finite-difference form⁶ with 20 levels represented over the altitude range 0–80 km, whilst in the horizontal domain fields are represented by a truncated series of spherical harmonics⁵. Martian topography is derived from the US Geological Survey Digital Terrain Model (DTM)⁷. The SGCM represents atmospheric radiative processes by newtonian relaxation (on a timescale of 3 sol (ref.8)) to a specified zonal mean temperature state as commonly used in simple model studies of the Earth’s atmosphere⁹. The temperature state used consists of a simple analytical function adapted to produce a time-mean state in the complete model which is similar to that of the NASA Ames GCM¹⁰ and to observations¹¹ of the martian atmosphere from Mariner 9. Surface drag is represented by Rayleigh friction in the lowest model level on timescale τ .

Simulations were carried out for atmospheric states representative of the two solstice seasons under low-dust conditions. We have studied the effect of varying surface drag over the range $0.2 \text{ sol} < \tau < 10 \text{ sol}$ as well as the sensitivity to differences in both model and topographic resolution.



Figures 1 and 2 show the presence of equatorial WBCs in simulations with $\tau = 10$ sol. One WBC lies on the eastern flank of the Tharsis Plateau, in Chryse Planitia at a longitude of $\sim 50^\circ \text{ W}$, as might be expected due to the large longitudinal gradient of topography there. The other lies on the eastern slopes of Syrtis Major, around longitude 80° E , although its magnitude is smaller in the southern summer case. Both currents are thought to be WBCs because (1) they disappear in control simulations with no topography and (2) their width changes with surface drag in the manner expected for WBCs. As the strength

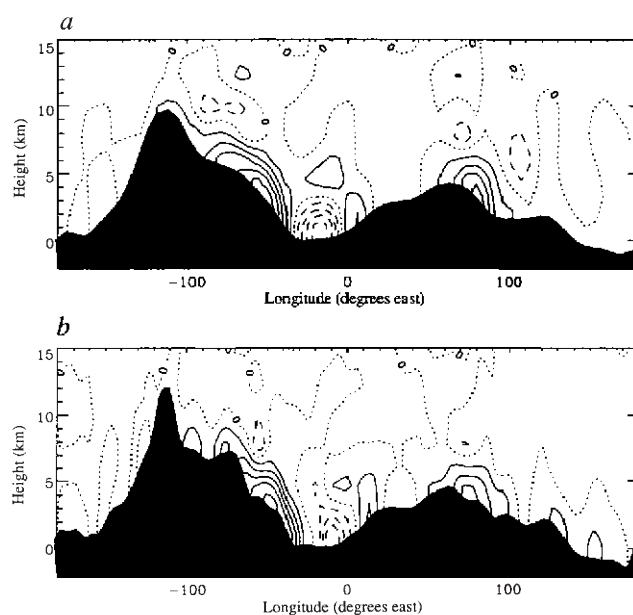


FIG. 2 A longitude–height plot for Mars, showing 15 sol time-mean meridional wind v (contours) in the lowest model σ -level ($\sim 1 \text{ km}$ above the surface), along the equator, during southern winter solstice, showing the two boundary currents at 50° W and 80° E . *a* and *b* show results from runs carried out at T21 and T42 resolution respectively; $\tau = 10$ sol in both cases. The return flow is evident at 20° W . The difference between topography resolved at T21 and at T42 is at its greatest in the longitude range 70° – 120° W and within the altitude range 10–15 km, where v is low. The large vertical amplitude of the topography should again be noted. (Contour intervals, 5.0 m s^{-1} , the zero contour is dotted, negative contours are dashed.)

of the Hadley cell in simulations of northern and southern summers is about the same, WBC intensity is similar, and the highest winds occur in the summer tropics in both cases (Fig. 1). More sophisticated models show that the Hadley cell is stronger in southern summer¹⁰, which would be expected to lead to more intense WBCs during this season. During both solstices, the martian tropical zonal mean meridional circulation is dominated by a single cross-equatorial Hadley cell, as is the case at the Earth's solstices¹². As the lower branch of this cell at the equator is concentrated into two WBCs, we expect martian WBCs to exert a strong influence on the flow within the Hadley cell.

Cross-equatorial flow can only happen when the flow departs from geostrophic balance (a simple balance between the pressure gradient and the Coriolis force on the flow), for example, owing to the effects of topography and/or surface friction. In our simulations, without topography, the meridional mass transport was augmented by $\sim 8\%$ on increasing the drag from $\tau = 10$ sol to $\tau = 0.2$ sol because larger surface friction enhanced cross-equatorial flow. In the presence of topography, longitudinal pressure torques may enable net north-south flow, in this case in the form of WBCs. Meridional transport in the SGCM was found to increase by 11% when surface drag was reduced from $\tau = 0.2$ sol to $\tau = 10$ sol owing to the greater strength of WBCs in the latter case.

It was found that the nature of the current was highly dependent on the surface drag timescale used, firstly because reducing

surface drag caused higher surface winds and secondly because the nature of the WBC changed from frictional control at $\tau = 0.2$ sol, to inertial control for $\tau \geq 1$ sol (Fig. 3). The width of the jet reached a minimum value at $\tau = O(1)$ sol (Fig. 3). For $\tau = 10$ sol, a significant southward return flow also occurs at low levels near longitude 20° W, though this feature is not present for $\tau = 2$ sol or less. The combined effect of narrowing and strengthening the WBC (each by a factor ~ 4 in going from $\tau = 0.2$ sol to $\tau = 10$ sol, see Fig. 3) evidently results in a small net increase in the global meridional transport. As the martian Hadley cell is thought to be the most important mechanism for transporting quantities such as heat or trace constituents across the equator¹⁰, it must be concluded that WBCs play a large part in cross-equatorial transport of constituents, especially those, such as water vapour, that are expected to be concentrated near the surface¹³.

We noted in experiments at T42 resolution (where Tn denotes a spherical harmonic expansion truncated at a total, longitudinal and latitudinal, wavenumber n) that the difference in circulation patterns and the strength of the Hadley cell between topography resolved at T21 and T42 respectively was negligible: WBCs

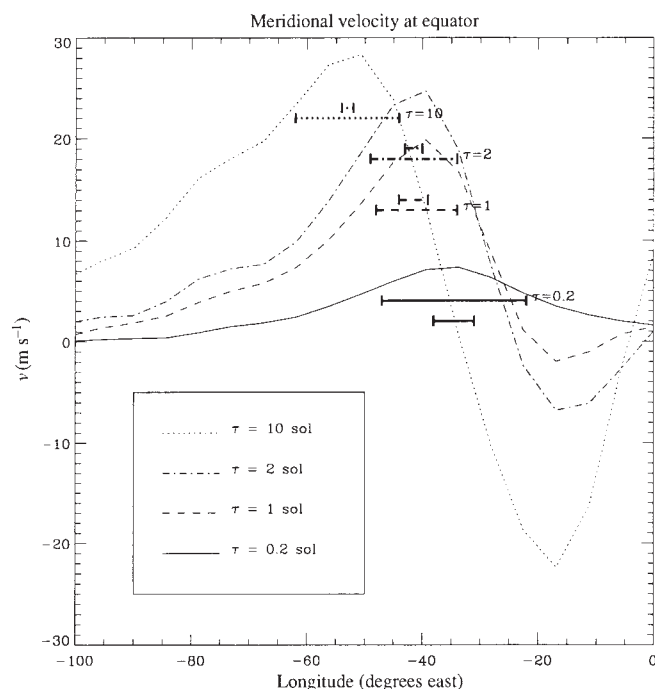


FIG. 3 The effect of surface drag on the simulation of the Tharsis WBC at southern winter solstice. All the simulations were carried out at model resolution T21, with values of τ set at 0.2, 1, 2 and 10 sol. Each curve of meridional wind, v , is accompanied by two bars, the linestyle of the two bars being the same as the curve to which they apply (for example, $\tau = 10$ is a dotted line and the two bars associated with it are dotted). Positive v indicates northward flow. The upper bar is the width the WBC would tend to if it was controlled purely by frictional forces and the lower bar is that expected if controlled purely by inertial forces. It can be seen that the width of the WBC produced with $\tau = 0.2$ sol is consistent with friction control and the widths of the other three cases are consistent with inertial control. Note that the centre of the WBC seems to move westward as friction is reduced.

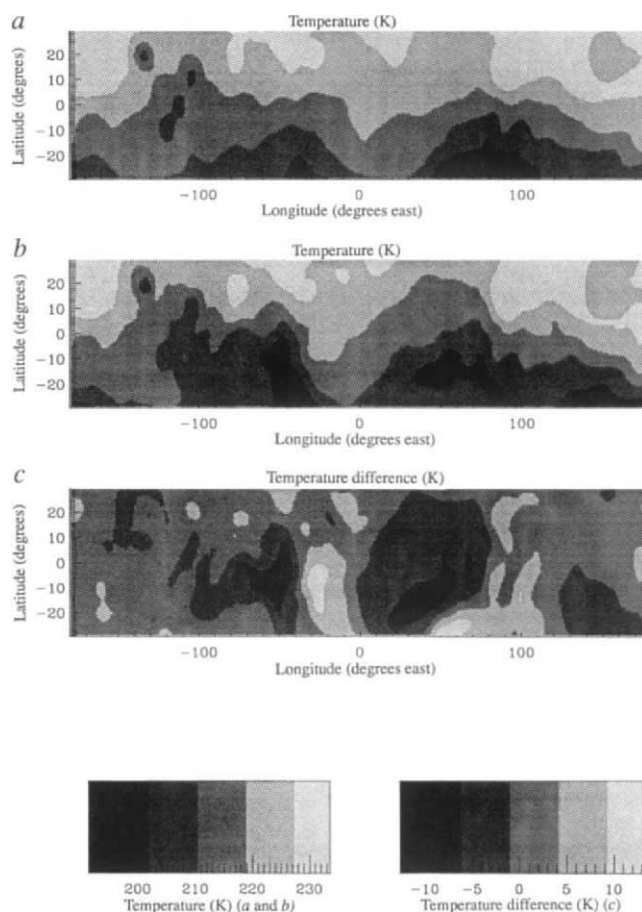


FIG. 4 Plots showing time-mean temperatures (shading) in the lowest model level. a, Run carried out at $\tau = 0.2$ sol, and b, at $\tau = 10$ sol. c, The difference $b - a$, caused mainly by advection of cold fluid northwards into the summer hemisphere by the Tharsis WBC at 50° W. (Note different temperature scale). The effect of the return flow is shown at 25° W and is evident as a hot area in c. The Syrtis Major WBC gives a far smaller signal. The model signal shown in the range $60^\circ - 20^\circ$ W in c has a temperature of ~ 20 K, reducing to ~ 2 K at ~ 3.5 km above the surface. This would be difficult to detect by conventional remote sounding instruments, unless it was possible to detect a corresponding time-mean surface temperature anomaly. It should certainly be measurable by a network of surface stations.

occurred in the same places and wind strengths were approximately the same. This is because the main differences in topography resolved at T21 and T42 occur in the altitude range 10–15 km, where meridional winds are low as it is the transition zone between the upper and lower branches of the Hadley cell (Fig. 2). Over a range of surface drag parameters the minimum width of WBCs were $\sim 15^\circ$ in longitude. Although T21 resolution was adequate to resolve this, it was suspected that it may not have been enough to resolve the jet's core. We discovered, however, that the wind strengths were similar in runs at both T42 and T21 resolution (Fig. 2).

On Mars, bright depositional dust streaks observed at middle to low latitudes are believed to form in late southern summer and autumn^{14–16}, and are thought to be representative of global scale winds³ during these times. The orientation of these streaks, when averaged over $5^\circ \times 5^\circ$ cells, imply north–south wind flow, and are especially coherent at $40\text{--}50^\circ$ W (ref. 17), which is consistent with the longitude and direction of the Tharsis WBC produced in a model simulation during southern summer (Fig. 1a). In addition, Haberle *et al.*¹⁸, when comparing a one-dimensional boundary layer model with winds inferred from measurements taken during the entry of the Viking Lander 1 probe (at 48° W, 22° N) in early northern summer, found large discrepancies in wind speeds and their rotation with height which would be explained by significant advection of cold fluid from the southeast. This result is consistent with the presence of WBCs.

Boundary current winds also advect cold fluid towards the equator from the winter tropics, which might lead to a temperature signal observable by future spacecraft missions. The SGCM produces a strong thermal signal near the surface (see Fig. 4), although its magnitude may be significantly larger than that actually observed because the model representations of boundary-layer processes (such as heat and momentum transfer) are very simple at present.

WBCs may have a crucial role to play in the generation of global or great dust storms, because dust raising is critically dependent on low-altitude wind strength¹⁹, which in turn is the result of the superposition of winds caused by different forcing mechanisms²⁰. This hypothesis is supported by the fact that large eastward-facing slopes in low latitudes are locations where global dust storms have commonly been seen to originate²¹ and these locations are coincident with the WBCs in our model.

Finally, it should be noted that the large diurnal temperature variation on Mars²² might cause a diurnal variation in the strength of the Hadley cell and hence in the strength of WBCs. Such effects are being investigated with a more sophisticated numerical model. \square

Received 23 September 1993; accepted 4 January 1994.

1. Anderson, D. L. *T. Globl atmos. Res. Progr. Pubs Ser.* **23**, 317–355 (1980).
2. Esposito, P. *et al.* in *Mars* (eds Kieffer, H. H., Jakosky, B. M., Snyder, C. W. & Matthews, M. S.) Ch. 7 (Arizona Univ. Press, Tucson, 1992).
3. Greeley, R., Skyeck, A. & Pollack, J. B. *J. geophys. Res.* **98**, 3183–3196 (1993).
4. Gill, A. E. *Atmosphere–Ocean Dynamics* 516–522 (Academic, San Diego, 1982).
5. Hoskins, B. J. & Simmons, A. J. *Quart. Jl. R. met. Soc.* **101**, 637–655 (1975).
6. Phillips, N. A. *J. Met.* **14**, 184–185 (1957).
7. *Atlas of Mars* (US geol. Surv. Topographic Ser. No. M 15M, Flagstaff, 1989).
8. Goody, R. & Belton, M. J. *Planet. Space Sci.* **15**, 247–256 (1967).
9. James, I. N. & Gray, L. J. *Q. Jl. R. met. Soc.* **112**, 1231–1250 (1986).
10. Haberle, R. M. *et al.* *J. geophys. Res.* **98**, 3093–3123 (1993).
11. Conrath, B. J. *et al.* *J. geophys. Res.* **78**, 4267–4278 (1973).
12. Lindzen, R. S. & Hou, A. Y. *J. atmos. Sci.* **45**, 2416–2427 (1988).
13. Jakosky, B. M. & Haberle, R. M. in *Mars* (eds Kieffer, H. H., Jakosky, B. M., Snyder, C. W. & Matthews, M. S.) Ch. 28 (Arizona Univ. Press, Tucson, 1992).
14. Greeley, R., Lancaster, N., Lee, S. & Thomas, P. in *Mars* (ed Kieffer, H. H., Jakosky, B. M., Snyder, C. W. & Matthews, M. S.) Ch. 22 (Arizona Univ. Press, Tucson, 1992).
15. Ward, A. W., Doyle, K. B., Helm, P. J., Weisman, M. K. & Witback, N. E. *J. geophys. Res.* **90**, 2038–2056 (1985).
16. Thomas, P., Ververka, J., Gineris, D. & Wang, L. *Icarus*, **60**, 161–179 (1984).
17. Kahn, R. A., Martin, T. Z., Zurek, R. W. & Lee, S. W. in *Mars* (eds Kieffer, H. H., Jakosky, B. M., Snyder, C. W. & Matthews, M. S.) 1042–1043 (Arizona Univ. Press, Tucson, 1992).
18. Haberle, R. M., Houben, H. C., Hertenstein, R. & Herdette, T. *J. atmos. Sci.* **50**, 1544–1559 (1993).
19. Greeley, R., Leach, R., White, B., Iversen, J. & Pollack, J. *Geophys. Res. Lett.* **7**, 121–124 (1980).
20. Leovy, C. B., Zurek, R. W. & Pollack, J. B. *J. atmos. Sci.* **30**, 749–762 (1973).
21. Martin, L. J. & Zurek, R. W. *J. geophys. Res.* **98**, 3221–3246 (1993).
22. Martin, T. Z. *Icarus* **45**, 427–446 (1981).

Assessing the pyroclastic flow hazard at Vesuvius

Flavio Dobran*†, Augusto Nerl††
& Micol Todesco§

* Department of Earth System Science, New York University,
New York, New York 10003, USA

† Istituto Nazionale di Geofisica, Via di Vigna Murata 605, Rome, Italy

‡ GNV, § Dipartimento di Scienze della Terra, Università di Pisa,
Via S. Maria 53, 56100 Pisa, Italy

IN large eruptions, Vesuvius has generated catastrophic avalanches of tephra and hot gases, such as those that destroyed Pompei and Herculaneum in AD 79, and Torre del Greco and surrounding towns in 1631^{1–12}. These avalanches (pyroclastic surges and flows) are produced from collapses of the eruptive column, and can travel at $>100\text{ m s}^{-1}$, with temperatures exceeding 800°C . In 1944 Vesuvius ended its most recent cycle of activity, which had begun with the explosive eruption of 1631. Here we use numerical simulations to assess the hazards posed by the pyroclastic flows that are likely to accompany the onset of the next cycle of activity. We examine three different scales of eruption, and use vent conditions established by modelling magma ascent along the conduit^{13,14}. Our results indicate that large- and medium-scale eruptions can produce complete destruction in the 7 km radius around the volcano (an area in which one million people live and work) in about 15 minutes or less, and that only small-scale eruptions can be arrested by the topographic relief of Monte Somma.

The Somma–Vesuvius complex has exhibited various types of activity over the past 35,000 yr (ref. 1). Large-scale plinian eruptions (Codola, Sarno, Basal, Greenish, Lagno Amendolare, Mercato, Avellino and Pompei) erupted several cubic kilometres of material and have occurred every few centuries to millennia, whereas medium-scale sub-plinian eruptions (AD 412 and 1631) have occurred every few centuries, with each erupting $\sim 0.1\text{ km}^3$ of material¹⁵. It appears that the smaller-scale strombolian and effusive events occurring every few decades normally follow the plinian and sub-plinian eruptions until the conduit closes, and that the plinian and sub-plinian eruptions occur from the closed-conduit states of the volcano¹². A common feature of the plinian eruptions is that they were interrupted intermittently as a result of partial column collapses producing pyroclastic surges and flows^{2,5}, and ended with the interaction of magma with water from underground aquifers^{2,9,16}. The plinian and sub-plinian eruptions from the Avellino eruption $\sim 3,400$ yr ago to AD 1631 are all characterized by the emission of highly differentiated magmas, trachytic or phonolitic in character^{17,18}. The pumice-fall deposits of Avellino, Pompei and the AD 1631 eruptions consist of white phonolite at the base and grey tephritic phonolite at the top^{11,19}. Some insight on the future activity of Vesuvius, and on its effects on the surrounding area, can be established from studies of its past behaviour and distribution of its products¹⁹. The results from this kind of study are, however, poorly constrained by thermodynamics, geophysics and thermofluid-dynamics, and a more precise assessment of the future behaviour of Vesuvius could be achieved by modelling the entire volcanic system¹².

The available volcanological and petrological data for Vesuvius have recently been used to model magma ascent during the AD 79 eruption^{13,20}. Based on the magma composition, temperature and crystal content, location of magma chamber, and stratigraphy, this modelling yielded likely values of conduit diameter, gas–pyroclast pressure and velocity distributions as a function of the mass discharge rate. The gas–pyroclast conditions at the vent were subsequently used in a physical model of the volcanic column¹⁴ to study pyroclastic flows caused by column collapses. This column model employs a subgrid-scale